

Wave signatures and electrostatic phenomena above aurora: Cluster observations and modeling

J. De Keyser,¹ R. Maggiolo,¹ M. Echim,^{1,2} and I. Dandouras³

Received 10 August 2010; revised 23 March 2011; accepted 31 March 2011; published 30 June 2011.

[1] This paper reports Cluster high-altitude observations above the acceleration region of a typical monopolar electric field event at the plasma sheet boundary. The observations reveal both characteristics of waves and signatures of electrostatic acceleration. The observations can be interpreted in terms of low-frequency transverse magnetic waves on the auroral interface. A reconstruction of the spatial structure across the interface, effectively correcting for the slow oscillations of the interface, allows a proper determination of the electric potential and of the upward and downward currents. Because of the long wave period, the auroral system can be understood in terms of a quasi-electrostatic model. In this model, the precipitating plasma sheet particles induce a perpendicular heating of cold ionospheric H^+ and O^+ ions. As these ions escape from the ionosphere, their perpendicular motion is converted into parallel motion in the divergent geomagnetic field as a result of the conservation of magnetic moment. These ions acquire an additional parallel energy through acceleration by the magnetic-field-aligned electric field in the auroral acceleration region. They also may gain substantial perpendicular energy due to the perpendicular electric field, as the $\vec{E} \times \vec{B}$ drift increases with altitude. Both types of acceleration are typical electrostatic phenomena.

Citation: De Keyser, J., R. Maggiolo, M. Echim, and I. Dandouras (2011), Wave signatures and electrostatic phenomena above aurora: Cluster observations and modeling, *J. Geophys. Res.*, 116, A06224, doi:10.1029/2010JA016004.

1. Introduction

[2] Quasi-stationary magnetosphere-ionosphere coupling models are able to describe both large-scale aurora [Chiu and Schulz, 1978; Lyons, 1980; Chiu and Cornwall, 1980] and smaller-scale discrete arcs [Lyons, 1981; Echim et al., 2007, 2008; De Keyser and Echim, 2010; De Keyser et al., 2010]. These models are based on the concept of a DC electric circuit connecting a magnetospheric generator to an ionospheric load via field-aligned currents; changes in the auroral circuit produced by variations in the generator or by modifications of the ionospheric conductivity are considered to be rather slow. This electric circuit is associated with the existence of field-aligned electric potential differences between a high-altitude electric potential structure at a magnetospheric boundary and the low-altitude ionospheric potential. The parallel potential difference is related to the field-aligned currents through the current-voltage relation. This parallel potential difference is also responsible for a downward acceleration of magnetospheric particles so that they precipitate as a rather monoenergetic population and produce auroral emission.

[3] Time-dependent models of aurora are based on the concept of magnetic perturbations traveling between the

magnetosphere and the ionosphere. Ionospheric feedback on the magnetosphere through reflected Alfvén waves and anomalous or turbulent resistivity may play a role in this interaction. Time-dependent models succeed in modeling auroral arcs and their multiplicity, with spatial scales of the order of tens of kilometers or less [e.g., Atkinson, 1970; Sato, 1978; Lysak, 1986; Knudsen, 2001; Lysak and Song, 2002; Keiling, 2009]. They are thought to provide a more realistic description of smaller-scale, shorter-duration arcs. Other types of wave-particle interaction may contribute to auroral acceleration, of particular interest being lower hybrid wave acceleration [Chang and Coppi, 1981].

[4] The electrostatic and wave mechanisms are not necessarily in contradiction, but may rather supplement each other [Rönnmark and Hamrin, 2000]. Spacecraft and rocket data provide experimental evidence that supports both electrostatic acceleration [e.g., Ergun et al., 1998] as well as wave particle interactions [e.g., Chaston et al., 2004]. In a recent analysis, Newell et al. [2010] have used DMSP data to quantify the contribution of the two types of aurora to the overall auroral energy input. Their results indicate that monoenergetic aurora, sustained by quasi-static acceleration, provides a larger energy input than the broadband (wave) acceleration aurora, but clearly both are important. The Cluster observations reported here demonstrate that electrostatic and wave phenomena can be present in the same event.

[5] The polar cap boundary (PCB) is a key region in the overall magnetospheric configuration, as it is often associated with the open/closed field line boundary [e.g., Siscoe

¹Space Physics Division, Belgian Institute for Space Aeronomy, Brussels, Belgium.

²Institute for Space Sciences, Bucharest, Romania.

³CESR-CNRS, Toulouse, France.

and Huang, 1985; Aikio et al., 2006; Hubert et al., 2010]. The PCB is therefore believed to be roughly the ionospheric foot point of the interface between the lobes and the plasma sheet. In ground-based radar data the PCB is identified by an observed spatial break in the F layer electron temperature due to the different types of precipitation on open and closed field lines [e.g., Aikio et al., 2006, 2008]. The radar PCB is located at or slightly poleward of the optical emission boundary at the poleward edge of the auroral oval, which separates the oval from the polar cap [Hubert et al., 2010]. Space-based in situ particle observations in low Earth orbit show the PCB as the transition between plasma sheet boundary layer (PSBL) precipitation and the polar rain [Aikio et al., 2008]. Space observations at higher altitudes, such as those by Cluster at geocentric distances of 5–7 R_E , indicate that this boundary is characterized by a monopolar electric field, that is, a perpendicular electric field with a definite polarity [Johansson et al., 2006]. Such a monopolar electric field corresponds to an essentially monotonic electric potential variation $\Delta_{\perp}\hat{\phi}$ across the magnetospheric interface. (Symbols with/without a hat denote magnetospheric/ionospheric quantities.) It is therefore not surprising that stable discrete arcs are observed near the PCB over a broad range of local times [Weber et al., 1991], as well as other auroral phenomena such as ion outflows and conics [Tung et al., 2001; Semeter et al., 2003; Aikio et al., 2008] and ELF/VLF electric and magnetic waves [Tsurutani et al., 2001].

[6] In situ observations of the auroral system by Cluster include electric field measurements by the EFW instrument [Gustafsson et al., 2001]. Traditionally, the high-altitude electric potential is obtained by integration along the spacecraft orbit [Vaivads et al., 2003; Johansson et al., 2006]. Field-aligned currents (FACs) are routinely obtained from the magnetic field measurements by the FGM magnetometer [Balogh et al., 1997, 2001]. In general, FACs cannot be computed with the curlometer [Dunlop et al., 2002] as FAC regions are typically thinner than the Cluster spacecraft separations. It is possible, in principle, to infer FACs from the magnetic field perturbations observed by a single spacecraft [Johansson et al., 2005]. However, these techniques of simply integrating the electric field along the orbit to obtain the electric potential profile and differentiating the magnetic field to obtain the FACs are not valid if the structure moves.

[7] FACs are mostly carried by electrons that are accelerated by a field-aligned potential drop $\Delta_{\parallel}\phi = \phi - \hat{\phi}$, where ϕ denotes the ionospheric potential and $\hat{\phi}$ the magnetospheric potential. The ions contribute to a lesser extent. Electron data are provided by the PEACE instrument [Johnstone et al., 1997] and ion distributions by the CIS spectrometer [Rème et al., 2001]. In general, conjugate low-altitude observations may offer complementary information on the auroral acceleration process and the electrodynamics of the auroral arc [e.g., Echim et al., 2009].

[8] This paper reports Cluster observations of a monopolar electric field event at the PCB showing both wave aspects and electrostatic properties (section 2). As the wave periods are rather low, a quasi-electrostatic model based on current continuity can explain these electrostatic properties, including the parallel and perpendicular energization of the

escaping ionospheric ions (section 3). The paper concludes with a discussion (section 4).

2. Observations of a Polar Cap Boundary Arc

[9] A strong monopolar electric field was observed at the lobe–plasma sheet interface by Cluster-1 on 28 February 2003, around 18:08:30 UT, at 5.6 R_E geocentric distance, near local midnight and at -73.5° invariant latitude. Johansson et al. [2006] cite this event as being typical for high-altitude monopolar electric field structures.

[10] The other Cluster spacecraft encounter similar structures about an hour later. The corresponding structures are readily identifiable as they correspond to passes from the lobe into the plasma sheet. They are similar in that none of the passes shows a detectable plasma on the lobe side (with CIS-CODIF, energy >10 eV), all of them show similar high-energy plasma sheet ion populations (with energies above 10 keV), and all are characterized by upgoing ions (energies around 100 eV). IMAGE EUV images indicate that the midnight auroral oval is fairly dynamic, so plasma sheet boundary structure is likely evolving considerably over a time scale of several minutes. Aikio et al. [2008] have conducted a detailed study of the PCB during four consecutive Cluster passes on 27 February 2004, and they also find changes both in the detailed PCB structure and in its environment; the spacecraft separations were much smaller during this event so that the time scale could be assessed to be only a few minutes.

2.1. Reference Frame Orientation

[11] Due to this time variability the reference frame has to be established with single-spacecraft methods. The interface must be essentially aligned to the magnetospheric magnetic field \vec{B} ; the average magnetic field during the event is $[-315, -75, -125]$ nT in GSE coordinates, which gives the \vec{z} direction of the reference frame. It is assumed here that the interface is a locally planar layer, something that is not evident a priori; it turns out to be a useful working hypothesis, although some of its limitations will be indicated later on. The orientation of this planar layer then remains to be determined: the interface normal \vec{x} must lie in the plane perpendicular to \vec{B} ; \vec{y} then follows automatically, lying inside the interface and being perpendicular to \vec{B} .

[12] A first possibility that can be explored is to consider minimum variance analysis of the magnetospheric electric field. In a planar discontinuity, there exists a variable electric field component only along the normal direction, so that \vec{x} would correspond to the maximum variance direction, while the other variances ideally would be zero. In reality one finds a zero variance along \vec{z} since the EFW parallel electric field is constant (zero) by design as the condition $\hat{E}_{\parallel} = 0$ is used to supplement the measured spin plane electric field components in order to obtain the full electric field vector [Gustafsson et al., 2001]. The two other components, however, have nonzero eigenvalues that are not too well separated, seeming to suggest that the layer cannot be considered planar. Minimum variance analysis of the magnetic field vector similarly leads to eigenvalues that are not well separated, and components indicating deviations from planarity. Minimum variance analysis therefore does not

give a conclusive answer as to the actual normal direction, even if the structure would be planar.

[13] Scanning through all possible orientations, however, one particular orientation manifests itself as being the most plausible, since only for that value a consistent interpretation of the event can be found. The reference frame is given by $\vec{\hat{x}} = [-0.415, +0.595, +0.688]$, $\vec{\hat{y}} = [+0.066, +0.774, -0.630]$, and $\vec{\hat{z}} = [-0.908, -0.216, -0.360]$, all expressed in the GSE frame; the orientation is precise up to a few degrees in the xy plane. There are a handful of independent arguments that support this choice of orientation, and these arguments will be discussed as the observations are presented.

[14] A first argument is evident from the vectors given above. Cluster-1 is located near local midnight above the southern auroral oval. The magnetic field direction $\vec{\hat{z}}$ is pointing along $-\vec{\hat{x}}_{\text{gse}}$ and $\vec{\hat{y}}$ is more or less along $+\vec{\hat{y}}_{\text{gse}}$, with the interface normal roughly in the GSE xz plane, i.e., just what is expected for the polar cap boundary near local midnight. This is, of course, only a qualitative justification of the chosen frame.

2.2. Time Profiles

[15] The Cluster-1 observations acquired on 28 February 2003 between 18:00:00 and 18:20:00 UT are summarized in Figure 1. The observations are given in the reference frame introduced above.

[16] The EFW instrument measures the two spin plane electric field components. To obtain the full electric field vector, it is assumed that the parallel electric field is zero, $\hat{E}_{\parallel} = 0$, which is reasonable since Cluster is at relatively high altitude and thus most likely above the top of the acceleration region [Mozer and Hull, 2001]. We have compared the EFW electric field measurements to the electric field obtained by the EDI instrument [Paschmann et al., 2001] in the lobe and to the convection electric field computed from the plasma and magnetic field data in the plasma sheet boundary. These electric fields agree very well, indicating that electric wake field effects [Engwall et al., 2006] do not play a role here. EFW provides data throughout the crossing, while there are no EDI data inside the transition because of the variability of the electric field, and while there are no reliable plasma data in the lobe because of the low count rates there as the spacecraft potential forms a barrier for the cold ions. The monopolar \hat{E}_x component perpendicular to the interface dominates the structure (Figure 1a). The tangential electric field \hat{E}_y , inside the interface, however, is relatively strong and cannot be ignored; its importance will be discussed later. As $\vec{\hat{z}}$ is along the magnetic field, \hat{E}_z is zero.

[17] The FGM magnetometer [Balogh et al., 1997, 2001] provides the magnetic field. In fact, one is more interested in the deviations $\delta\vec{B}$ from the background magnetospheric field since these carry information on the geometry of the interface and on the field-aligned currents. From the EFW data, it is clear that we are looking for a structure that is crossed in the time span of a few minutes. To remove the effect of the background magnetic field, a detrending procedure was applied in which the running field average over 300 s, a time scale longer than the event duration, was subtracted from the total field to obtain $\delta\vec{B}$, shown in Figure 1b.

[18] Figures 1c–1e show differential energy flux spectrograms for the upward, perpendicular, and downward moving

electrons observed by the PEACE instrument [Johnstone et al., 1997]. PEACE records an intense cold photoelectron distribution throughout the whole region (visible close to the bottom of each of the three spectrograms). On the plasma sheet side (equatorward of the boundary, $\hat{x} > 0$) an intense hot electron distribution of plasma sheet origin is observed with energies of 1–10 keV, with a predominantly downward flux. The hot electrons appear to be present also some distance into the lobe, but with a much reduced density. Inside the interface, one distinguishes two regions. Between 18:07:50 and 18:09:40 UT, one finds predominantly upflowing electrons with energies of 50–100 eV, but with a lot of fine-scale structure. From 18:09:40 UT on, the hot plasma sheet electrons show an intense downward flux. As the electrons are the main current carriers, one can associate both regions roughly with the downward and upward current regions.

[19] Figures 1f–1m show CIS/CODIF data [Rème et al., 2001]. The differential number flux spectrograms of H^+ and O^+ ions as a function of energy and pitch angle (Figures 1f–1i) show that the spacecraft is first located in the magnetospheric lobe where no ions above 30 eV are detected, although there is likely an ion population too cold for CIS/CODIF to detect [Engwall et al., 2006]. Later on, when Cluster enters the plasma sheet, it records successive injections of hot plasma sheet ions above 2.5 keV. These are composed of a rather isotropic H^+ population with densities around 0.15 cm^{-3} and energies around 10 keV, with a small fraction of O^+ . Note that a fraction of the hot ions has energies above the CIS/CODIF upper limit and is missed by the instrument. At the same time, warm ions are detected with energies of 0.1–5 keV and a temperature of a few hundred eV. There is a relatively large admixture of O^+ , hinting at an ionospheric origin. Such ionospheric outflows are not uncommon at the PCB [e.g., Aikio et al., 2008]. In the lobe–plasma sheet interface these ionospheric ions have pitch angles near 90° (perpendicular motion) that later on, some distance into the plasma sheet, get close to 0° (upward field-aligned motion). Figures 1j–1m give the density and the velocity of the H^+ and O^+ ions. The ionospheric H^+ and O^+ densities are comparable and largest in the return current region. The perpendicular velocity components $\hat{v}_{\perp x}$ and $\hat{v}_{\perp y}$ of H^+ and O^+ are similar and coincide very well with the electric drift $\vec{v} = \vec{E} \times \vec{B}/B^2$. The parallel speeds are small inside the interface, peak in the upward current region, and remain significant further into the plasma sheet, with the H^+ parallel speed a few times that of O^+ . The velocities are quite accurate for the O^+ population as the contribution from magnetospheric O^+ is negligible and also because the ionospheric O^+ forms a narrow beam whose velocity can be determined precisely.

[20] This is illustrated by the Cluster-1 CIS/HIA ion velocity distribution measured on 28 February 2003, around 18:08:23 UT, near the center of the time interval (Figure 2). The distribution is plotted in the $(\hat{v}_{\perp}, \hat{v}_{\parallel})$ plane. Since the HIA spectrometer performs a scan of energy space without mass discrimination, the ion velocity distributions are computed with the assumption that all ions are H^+ . Figure 2 shows three contributions. First, there is the hot H^+ distribution forming an almost spherical shell in velocity space, corresponding to a narrow high-energy

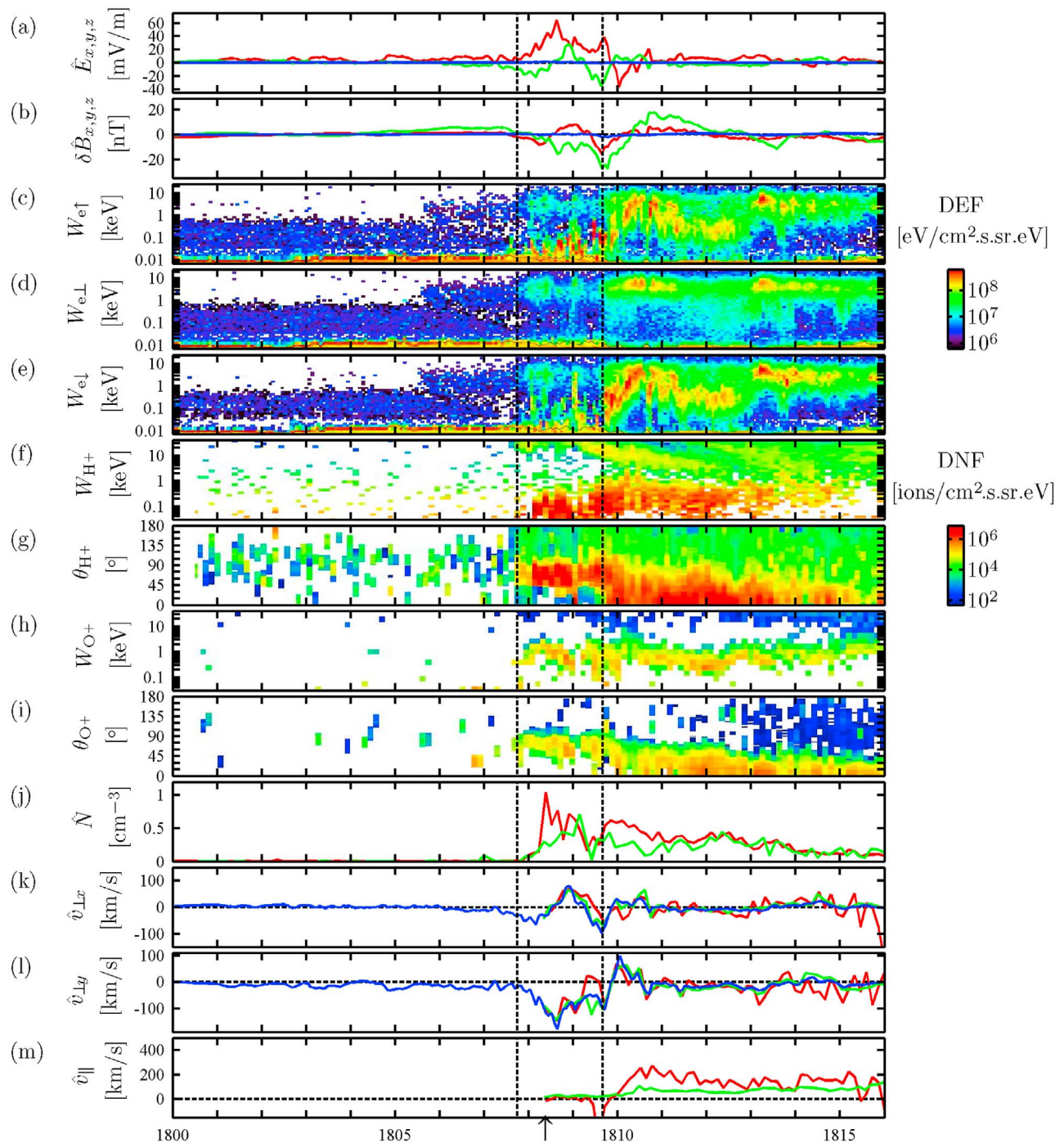


Figure 1. Cluster-1 observations on 28 February 2003, 18:00–18:16 UT, of the lobe–plasma sheet interface at $5.6 R_E$ geocentric distance and -73.5° invariant latitude. The data are shown in a stationary frame with \hat{x} along the interface normal and \hat{z} along the magnetic field. The arrow indicates the time corresponding to the velocity distribution shown in Figure 2. The vertical lines at 18:07:50 and 18:09:40 UT identify the edge of the downward current region and the boundary between the upward and downward current regions, respectively. (a) Electric field \hat{E}_x perpendicular to the arc (red), \hat{E}_y along the arc (green), and \hat{E}_z along the magnetic field (blue). (b) Magnetic field fluctuations $\delta\hat{B}_x$ (red), $\delta\hat{B}_y$ (green), and $\delta\hat{B}_z$ (blue). (c–e) Upward, perpendicular, and downward electron differential energy flux. H^+ differential number flux as a function of (f) energy and (g) pitch angle. O^+ differential number flux as a function of (h) energy and (i) pitch angle. (j) Magnetospheric density \hat{N} of 30 eV to 2.5 keV H^+ (red) and 30 eV to 5 keV O^+ (green) of ionospheric origin. (k) Magnetospheric perpendicular velocity component $\hat{v}_{\perp x}$ of H^+ ions (red) and of O^+ ions (green) and the electric drift (blue). (l) Idem for $\hat{v}_{\perp y}$. (m) Magnetospheric parallel velocity of H^+ ions (red) and O^+ ions (green).

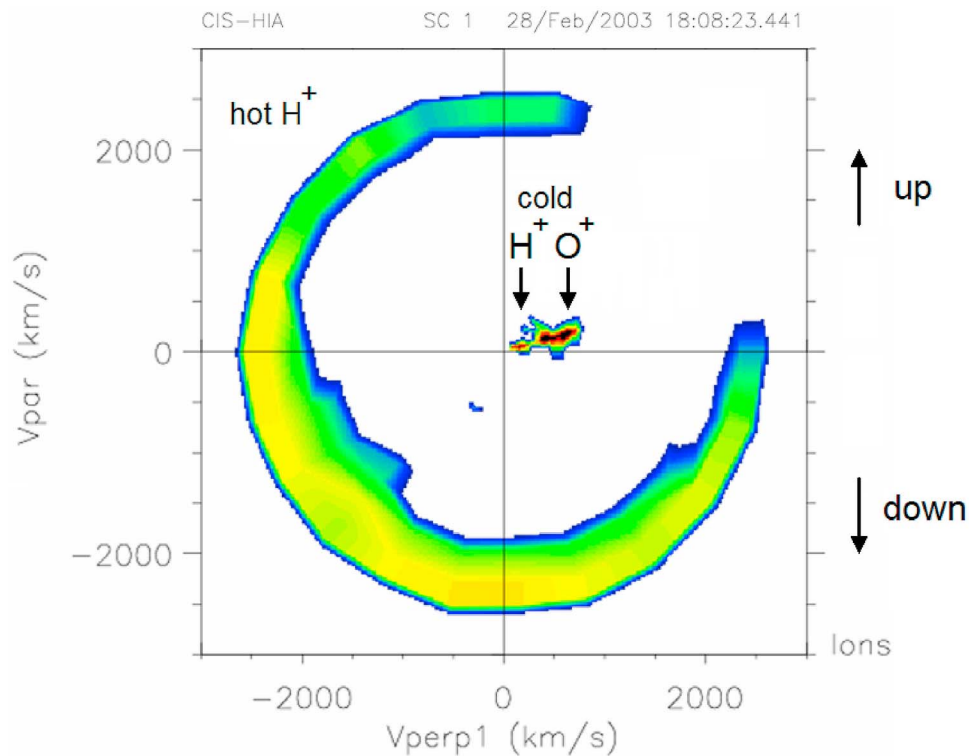


Figure 2. Cluster-1 CIS/HIA ion velocity distribution on 28 February 2003, around 18:08:23 UT, near the center of the time interval considered. The distribution is plotted in the v_{\perp} , v_{\parallel} plane and shows three contributions: (1) hot H^+ ions forming a shell with a narrow high-energy range with predominantly downward flux; (2) cold H^+ ions with a small positive v_{\parallel} and with a $v_{\perp} \approx 30$ km/s; and (3) cold O^+ ions with a small positive v_{\parallel} and with an apparent $v_{\perp} \approx 120$ km/s. Because of the assumption that all ions have the proton mass needed to compute velocity distributions from CIS/HIA (which has no mass discrimination), the O^+ velocities are four times too high (the square root of the O^+/H^+ mass ratio): in reality, all ions have the same perpendicular $\vec{E} \times \vec{B}$ drift of around 30 km/s.

range: these are the hot ions of plasma sheet origin, with predominantly downward flux. This type of distribution is typical of injected plasma sheet particles [see, e.g., *Eliasson et al.*, 1994, Figure 3b]. Second, Figure 2 shows the cold H^+ ions of ionospheric origin, with a small but positive \hat{v}_{\parallel} , and with a $\hat{v}_{\perp} \approx 30$ km/s that reflects the electric drift. Third, there is a cold O^+ population. Because of the assumption that all ions are H^+ , the velocity distribution function assigns O^+ ions a velocity that is four times too high (the square root of the O^+/H^+ mass ratio): again a small positive \hat{v}_{\parallel} , and a $\hat{v}_{\perp} \approx 120$ km/s, which in reality is also around 30 km/s, illustrating that all ions share the same perpendicular drift. This drift is too small to be easily discernible for the hot H^+ population.

2.3. Reference Frame Motion

[21] In order to understand the structure of the interface and of the auroral current system that is associated with it, one should study the event in a reference frame tied to the interface. Here, such a frame is established.

[22] Figure 1 indicates that both \hat{v}_x and the $\delta\hat{B}_x$ are non-zero inside the interface. If the interface is of the tangential discontinuity type, aligned with the magnetic field, this indicates the presence of a deviation from planarity. The

repeated sign changes of \hat{v}_x and $\delta\hat{B}_x$ can be interpreted as being the signatures of waves. Figure 3 (left) sketches the implications of transverse waves in the $\hat{x}\hat{z}$ plane that travel along the magnetic field. Maximum transverse speed \hat{v}_x is found where the magnetic field vector is tilted most, i.e., where the magnetic field excursion $\delta\hat{B}_x$ is maximum. If the wave propagates parallel/antiparallel relative to the field, there is an anticorrelation/correlation between \hat{v}_x and $\delta\hat{B}_x$. Figure 3 (right) shows a correlation plot of these two quantities. The correlation is made using the H^+ , O^+ , and electric drift speed for \hat{v}_x . There is indeed a positive correlation, as expected for the Southern Hemisphere where the waves should be traveling downward from the magnetosphere toward the ionosphere. Since the plasma velocities are essentially drift velocities, there must also be a correlation between the profiles of $\delta\hat{B}_x$ and $\hat{E}_y \approx \hat{v}_x/\hat{B}_z$, which is clearly visible in Figure 1. The observed magnetic field excursions $\delta\hat{B}_x$ of up to 15 nT, superimposed on a background field $\hat{B}_z = 340$ nT, correspond to a field line tilt of at most 2.5° , so the deviation from planarity is limited.

[23] Since plasma beta is low ($\beta < 0.01$) throughout this event, all characteristic magnetohydrodynamic waves propagate with essentially the Alfvén speed. The magnetospheric

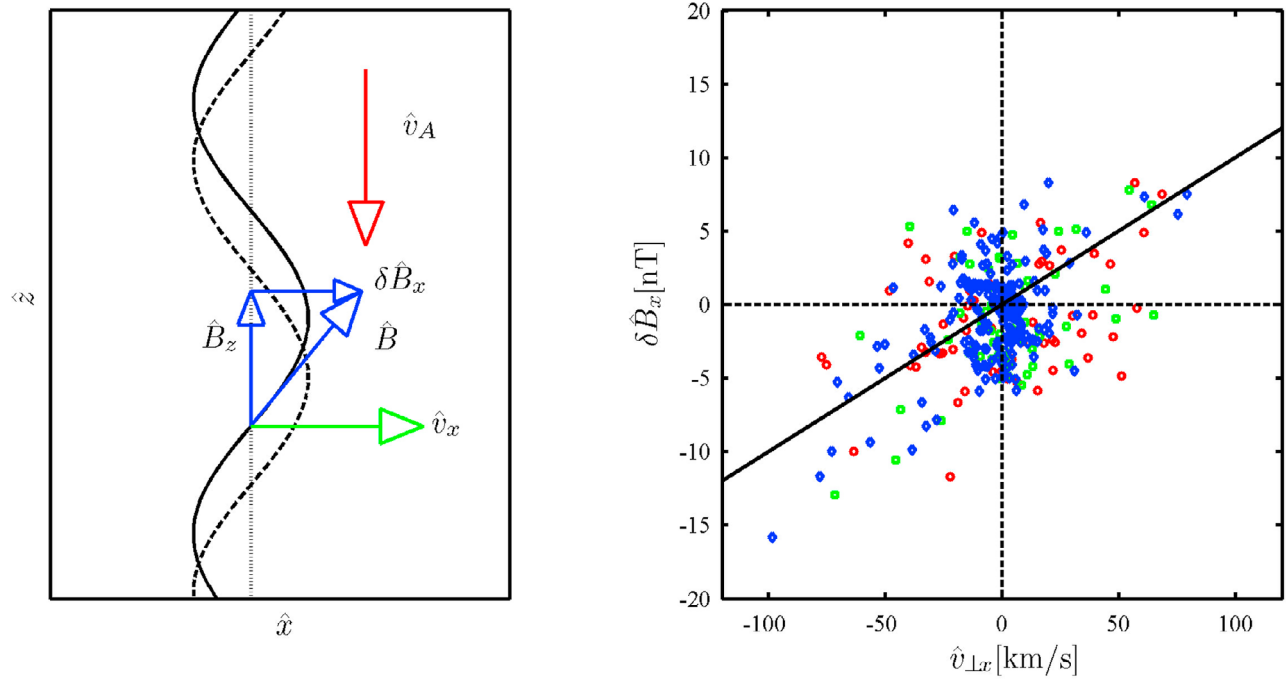


Figure 3. Signature of waves traveling along the magnetic field lines in a configuration representative of the Southern Hemisphere where the magnetic field points upward. (left) Antiparallel propagation implies a positive correlation between $\delta\hat{B}_x$ and \hat{v}_x . (right) This correlation is observed in the 28 February 2003 event. Three types of \hat{v}_x observations are depicted: H^+ velocity (red), O^+ velocity (green), and electric drift velocity (blue).

Alfvén speed \hat{v}_A can be computed in different ways. First, the expression

$$\hat{v}_A = \frac{\hat{B}}{\sqrt{\mu_0 \hat{\rho}}} \quad (1)$$

can be evaluated inside the transition, where the mass density $\hat{\rho}$ is dominated by the upflowing O^+ ; one obtains values around 3400 km/s. A second method to obtain the Alfvén speed is through

$$\hat{v}_A = \frac{\hat{E}_y}{\delta\hat{B}_x}; \quad (2)$$

with $\hat{E}_y = 25$ mV/m and $\delta\hat{B}_x = 8$ nT at the center of the return current region, this gives 3125 km/s. Yet another estimate comes from

$$\frac{\max \hat{v}_x}{\hat{v}_A} = \frac{\max \delta\hat{B}_x}{\hat{B}}, \quad (3)$$

from which $v_A \approx 3000$ km/s for $\max \hat{v}_x = 80$ km/s, $\max \delta\hat{B}_x = 8$ nT, and $\hat{B} = 340$ nT at the center of the interface. The different estimates all agree, lending confidence to the wave interpretation.

[24] The consistent interpretation of variations of magnetic field fluctuations along \hat{x} and electric field fluctuations in \hat{y} is a strong argument that supports our choice of reference frame orientation: for a different orientation, the correlation would vanish and it would become impossible to arrive at consistent estimates of the Alfvén velocity.

[25] The wave period visible in the \hat{v}_x , $\delta\hat{B}_x$, and \hat{E}_y time profiles is about 100 s. That would imply a wave length of $50 R_E$ if v_A would remain constant along the field line; the latter is not true, of course, but it clear that the wave length is very long. The conclusion therefore is that this interface can be regarded as an essentially planar field-aligned layer that is moving back and forth on a 100 s time scale. We will assume that the boundary velocity is given by

$$\hat{v}_{\text{bdry},x} = \hat{v}_x, \quad (4)$$

i.e., that the velocity of the boundary coincides with the instantaneously measured plasma velocity (or electric drift velocity) as would be the case for an incompressible slab. We will then use a comoving frame, i.e., a reference frame that is tied to the moving interface. In addition to the motion along \hat{x} , the frame also slides along the interface with $\hat{v}_{\text{bdry},y} = 15$ km/s.

[26] The changing position of the boundary as a function of time can be found from

$$\hat{x}_{\text{bdry}}(t) = \int_{\tau=t_0}^t \hat{v}_{\text{bdry},x}(\tau) d\tau + \hat{x}_{\text{bdry}}(t_0), \quad (5)$$

where $\hat{x}_{\text{bdry}}(t_0)$ represents an arbitrarily chosen reference position at a chosen time t_0 .

[27] Figure 4 shows the observations in the comoving frame. The boundary velocity $\hat{v}_{\text{bdry},x}$ is taken to be the normal component of the $\vec{E} \times \vec{B}$ drift (Figure 4a). The electric drift is known with a good accuracy and time resolution throughout the whole time interval, which makes it

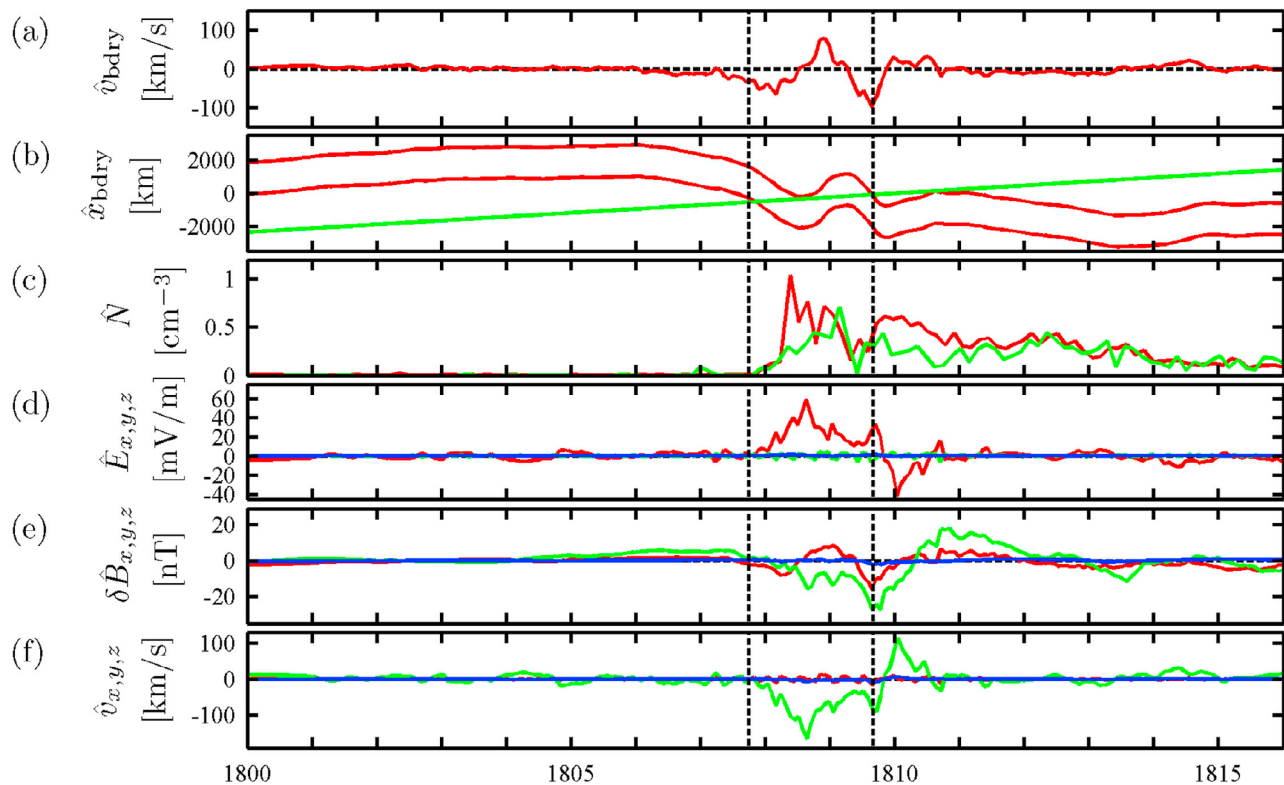


Figure 4. Cluster-1 observations on 28 February 2003, 18:00–18:16 UT, of the lobe–plasma sheet interface in the plasma rest frame (i.e., comoving with plasma in and near the boundary) with \hat{x} along the interface normal and \hat{z} along the magnetic field. The vertical lines at 18:07:50 and 18:09:40 UT identify the edge of the downward current region and the boundary between the upward and downward current regions, respectively. (a) Boundary velocity $\hat{v}_{\text{bdry},x}$ taken to be the normal component of the $\hat{E} \times \hat{B}$ drift. (b) Position of the boundary in the normal direction, with the lobe corresponding to $\hat{x} < 0$ and the plasma sheet to $\hat{x} > 0$. The position of two surfaces is shown in red, the poleward edge of the downward current region and the interface between the upward and downward current regions. The spacecraft position is traced by the green line. (c) For reference, the profiles of magnetospheric density \hat{N} of 30 eV to 2.5 keV H^+ (red) and 30 eV to 5 keV O^+ (green) indicate how the entrance of the spacecraft into the return current region corresponds to a high density, while in the upward current region the density falls back to low values as the ionospheric outflow diminishes. (d) In the interface frame that moves with $\hat{v}_{\text{bdry},x}$, only \hat{E}_x is nonzero. Note that $\hat{E}_x = 0$ away from the interface because of an appropriately chosen frame motion $\hat{v}_{\text{bdry},y}$. (e) Magnetic field fluctuation $\delta\hat{B}_x$ (red) reflects the frame motion in the normal direction, while $\delta\hat{B}_y$ (green) varies systematically as the spacecraft moves through the field-aligned current regions. (f) In the comoving frame, the electric drift only has a nonvanishing \hat{v}_y component (green) that reflects the role of \hat{E}_x .

possible to perform the integration implied in equation (5) with sufficient accuracy. The resulting boundary position $\hat{x}_{\text{bdry}}(t)$ is shown in Figure 4b, together with the spacecraft position $\hat{x}_{\text{sc}}(t)$. The lobe corresponds to $\hat{x} < 0$ and the plasma sheet to $\hat{x} > 0$. The position of two surfaces is given, one that corresponds to the poleward edge of the downward current region, and one that represents the interface between the upward and downward current regions. One can clearly see how the boundary position is changing rapidly, and nonmonotonically, as Cluster-1 passes through. The boundary oscillates over a distance of 1500 km and more during the crossing. It is interesting to relate the geometrical context provided by Figure 4b to the profiles of plasma density, electric field, magnetic field, and drift velocity (Figures 4c–4f). In the comoving frame the electric field has

only an \hat{E}_x component: clearly this is a monopolar positive electric field. Note that $\hat{E}_x = 0$ away from the interface because of the appropriately chosen $\hat{v}_{\text{bdry},y}$. In the comoving frame the plasma drift only has a \hat{v}_y component, which reflects the behavior of \hat{E}_x .

2.4. Spatial Profiles

[28] Once $\hat{x}_{\text{bdry}}(t)$ is computed, and knowing the spacecraft position $\hat{x}_{\text{sc}}(t)$, it is possible to plot all observations as a function of $\hat{x}_{\text{sc}}(t) - \hat{x}_{\text{bdry}}(t)$, the relative distance between the spacecraft and the interface, as shown in Figure 5. In this way, spatial profiles across the interface are obtained, at least in principle. In practice, such plots result in a “cloud” of data points scattered around some average profile. Note that this technique of using the normal boundary velocity to

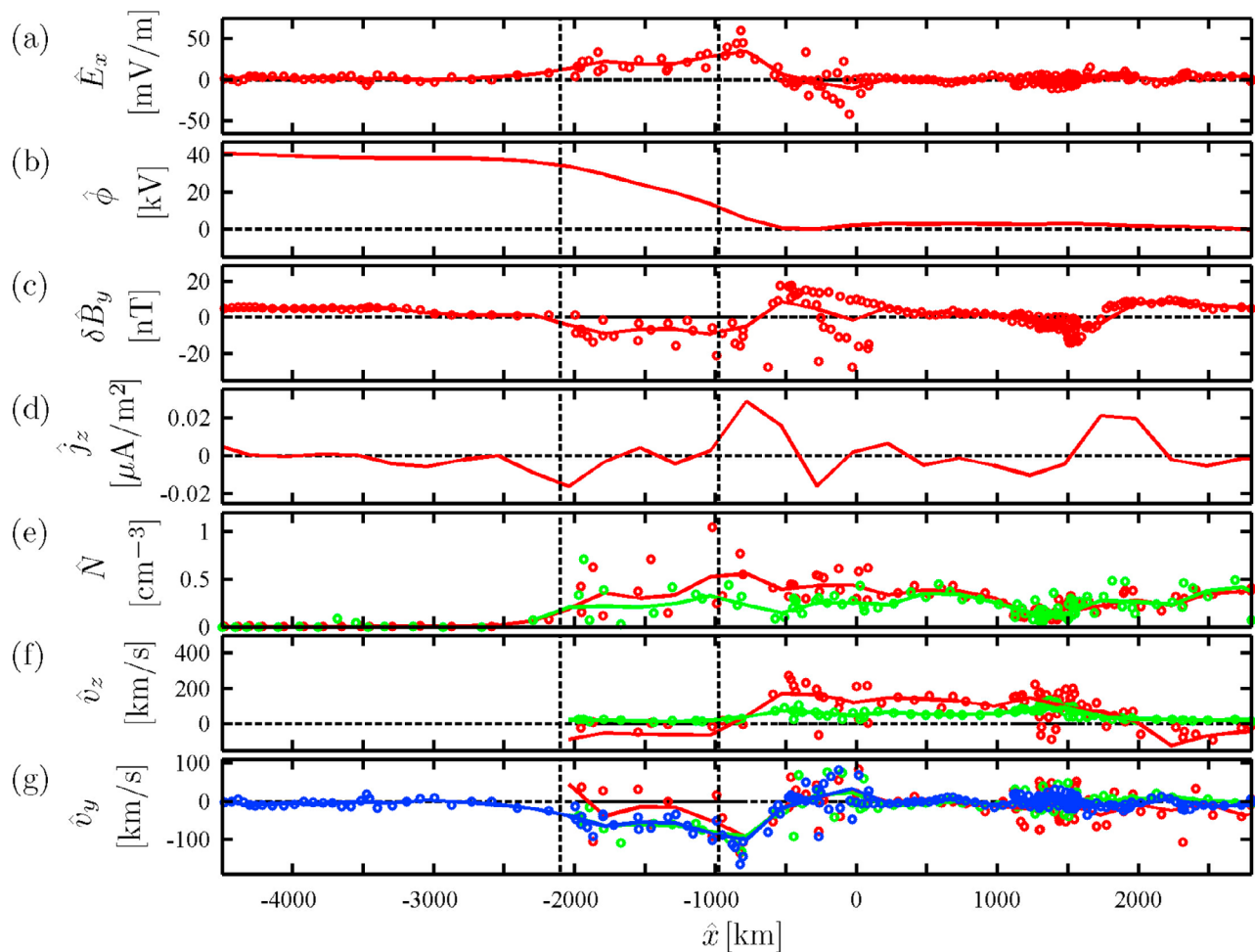


Figure 5. Cluster-1 observations on 28 February 2003, 18:00–18:16 UT, of the lobe–plasma sheet interface in the comoving frame with \hat{x} along the interface normal and \hat{z} along the magnetic field, plotted as a function of \hat{x} . The vertical lines at -2100 and -975 km identify the edge of the downward current region and the boundary between the upward and downward current regions, respectively. Symbols represent measurement points, and the continuous curves are “average” profiles. (a) Perpendicular electric field \hat{E}_x and (b) the corresponding electric potential profile $\hat{\phi}$. (c) Magnetic field fluctuation $\delta\hat{B}_y$ and (d) the corresponding field-aligned current \hat{j}_z . Note how the upward and return currents coincide with the edges of the monopolar electric field region. (e) Magnetospheric density \hat{N} of 30 eV to 2.5 keV H^+ (red) and 30 eV to 5 keV O^+ (green). (f) Parallel velocity \hat{v}_z of H^+ (red) and O^+ (green). (g) Velocity \hat{v}_y , along the structure for H^+ (red) and O^+ (green) and from the electric drift (blue).

deconvolve the time profiles has been used successfully in the context of the study of the moving magnetospheric boundary, and is called “empirical reconstruction” [see, e.g., Paschmann *et al.*, 1990; De Keyser *et al.*, 2005].

[29] Figure 5 shows that the magnetospheric interface thickness is on the order of 1500 km. That is quite large and should be compared to the hot H^+ gyroradius of 70 km, suggesting that this interface might actually be a composite one. From the monopolar electric field \hat{E}_x (Figure 5a) one can then compute the electric potential variation across the structure (Figure 5b) through

$$\hat{\phi}(\hat{x}) = - \int \hat{E}_x(\hat{x}) d\hat{x}; \quad (6)$$

a potential drop of around $\Delta_{\perp}\hat{\phi} = -40$ kV is obtained. That is very large. Note that this way of computing the electric potential variation is quite different from the straightforward along-track integration performed by Johansson *et al.* [2006, Figure 1], which yields $\Delta_{\perp}\hat{\phi} = -12$ kV. That procedure, however, does not account for the motion of the structure. Since the boundary motion is so fast, it is not surprising that we obtain a bigger potential difference. It should be noted that this auroral boundary crossing is one of the strongest electric field events observed [Johansson *et al.*, 2006]. Also, electric potential differences of several tens of kV are known to occur in the tail (e.g., the cross-tail potential [see Haaland *et al.*, 2008]).

[30] Similarly, the spatial profile of the magnetic field perturbation $\delta\hat{B}_y$ can be traced (Figure 5c), although there is

a substantial spread around the average profile. The fact that $\delta\hat{B}_y < 0$ inside the interface can be attributed to the field-aligned currents. Indeed, in a one-dimensional planar interface (an assumption that is now known to be correct to within a few degrees of magnetic field tilt) in which time variations are slow (which is justified as well), Ampère's Law states that

$$\hat{j}_z(\hat{x}) = \frac{1}{\mu_0} \frac{d\delta\hat{B}_y(\hat{x})}{d\hat{x}}. \quad (7)$$

In this way, the FACs can be computed. Figure 5d indicates $\hat{j}_z < 0$ on the lobe side and $\hat{j}_z > 0$ on the plasma sheet side of the structure, which agrees with the particle observations and also with the nature of the monopolar potential profile [De Keyser *et al.*, 2010]. Again, this computation differs from that of Johansson *et al.* [2006, Figure 3], who do not account for boundary motion.

[31] Figures 5e–5g summarize the ion data. An enhanced density is found in the return current region. The parallel velocity is small inside the return current region, while it is maximum in the upward current region. The perpendicular velocity is again simply the electric drift.

[32] It is not evident a priori that it is indeed possible to obtain sensible spatial profiles at all. The fact that such profiles can be reconstructed is a major argument in favor of our choice of reference frame orientation. For different directions of \hat{x} , one either obtains a shapeless “cloud” of data points, or structures that stretch over a wider distance and that would correspond to absurdly high values of $\Delta_{\perp}\phi$.

[33] The fact that the FACs computed from $\delta\hat{B}_y$ correspond nicely to the upward and downward current regions identified from the electron spectrograms forms another, independent, confirmation of the appropriateness of the choice of reference frame orientation.

3. A Quasi-Electrostatic Model

[34] The quasi-electrostatic picture describes the auroral current circuit in terms of a magnetospheric interface that is coupled to the ionosphere through FACs j_z , which close in the ionosphere as a height-integrated Pedersen current I_p [e.g., Lyons, 1980, 1981]. As time goes by, the FACs modify the magnetospheric interface as well as the ionosphere, but the magnetospheric interface may be able to maintain a quasi-static dynamic equilibrium [Roth *et al.*, 1993; De Keyser, 1999].

[35] There are several time scales that characterize the system. Assuming the distance between the ionosphere and the magnetosphere at Cluster altitude to be $5 R_E$, and neglecting the altitude variation of the propagation speeds, we find that (1) the Alfvén wave traveling time between magnetosphere and ionosphere is ~ 10 s as deduced from an Alfvén speed of ~ 3000 km/s obtained earlier; (2) the traveling time of hot precipitating electrons with energies above 1 keV is less than 2 s; (3) the transit times of hot H^+ and O^+ ions of 10 keV are 20 s and 80 s, respectively; (4) the time scale for upgoing ~ 100 eV electrons in the return current region is 20 s; and (5) the time scales for upgoing 1 keV H^+ and O^+ ionospheric ions are 60 s and

240 s, respectively. We ignore changes in the ionospheric state, which would introduce an additional time scale.

[36] The use of an electrostatic model is justified if the high-altitude source does not vary faster than the time needed to set up an equilibrium configuration, i.e., the longest of the characteristic time scales estimated above. In the present case, a quasi-electrostatic description can therefore be applied if the source changes on a time scale of a few minutes or longer; the quasi-static assumption would break down first for the cold upgoing ions. The wave period of 100 s is at the limit of quasi-stationarity. In order to find out how well the quasi-electrostatic model can describe the PCB, we will attempt to reproduce the observations using a fairly simple one-dimensional electrostatic model.

3.1. Description of the Model

[37] The auroral current circuit can be studied with a one-dimensional model based on current continuity [Lyons, 1980, 1981]. This model assumes that all horizontal currents are found below an altitude that corresponds to the top of the ionosphere; an altitude $h = 400$ km is adopted here. Any changes in the height-integrated horizontal Pedersen current I_p are then due to parallel currents j_z , taken here to be vertical and positive for upward currents. Let x denote the equatorward horizontal transverse coordinate, measured at the top of the ionosphere. The high-altitude positions \hat{x} are mapped to x by following the magnetic field lines. All magnetospheric profiles can then be expressed in terms of x . Note that the horizontal currents are Pedersen currents: the Hall currents are tangential to the arc and do not contribute to FAC closure in a one-dimensional geometry. The steady current continuity equation then is

$$-\frac{d}{dx}I_p = \frac{d}{dx}\left(\Sigma_p \frac{d}{dx}\phi\right) = j_z, \quad (8)$$

where Σ_p is the height-integrated Pedersen conductivity. Typically both Σ_p and j_z depend on the plasma properties and on the potential difference $\Delta_{\parallel}\phi$ along magnetic field lines between the ionosphere and the magnetosphere. The current-voltage specifies which field-aligned current densities j_z flow in response to $\Delta_{\parallel}\phi$. It should capture the physics of electrostatic acceleration, mirroring, and overall charge neutrality along field lines [e.g., Knight, 1973; Lemaire and Scherer, 1973; Fridman and Lemaire, 1980; Vedin and Rönnmark, 2005]. The description of Σ_p should account for the effects of solar illumination, precipitation, ionospheric neutral winds and ionospheric chemistry. We use here less detailed phenomenological descriptions. The overall structure of the model is illustrated in Figure 6.

[38] Let us first analyze the geometry of the event on 28 February 2003. Using a dipole magnetic field model for the relatively low geocentric distances involved, the field line on which the PCB is located is characterized by an invariant latitude $\Lambda = 73.5^\circ$, which corresponds to $L = 1/\cos^2 \Lambda = 12.4$. Because of the conservation of magnetic flux, the ratio of the ionospheric magnetic field strength B over the magnetospheric field strength \hat{B} equals the ratio of the magnetospheric over the ionospheric cross section of a flux tube. This ratio can be written as $B/\hat{B} = b_n b_r$, where b_n is the geometric mapping factor for distances normal to the PCB

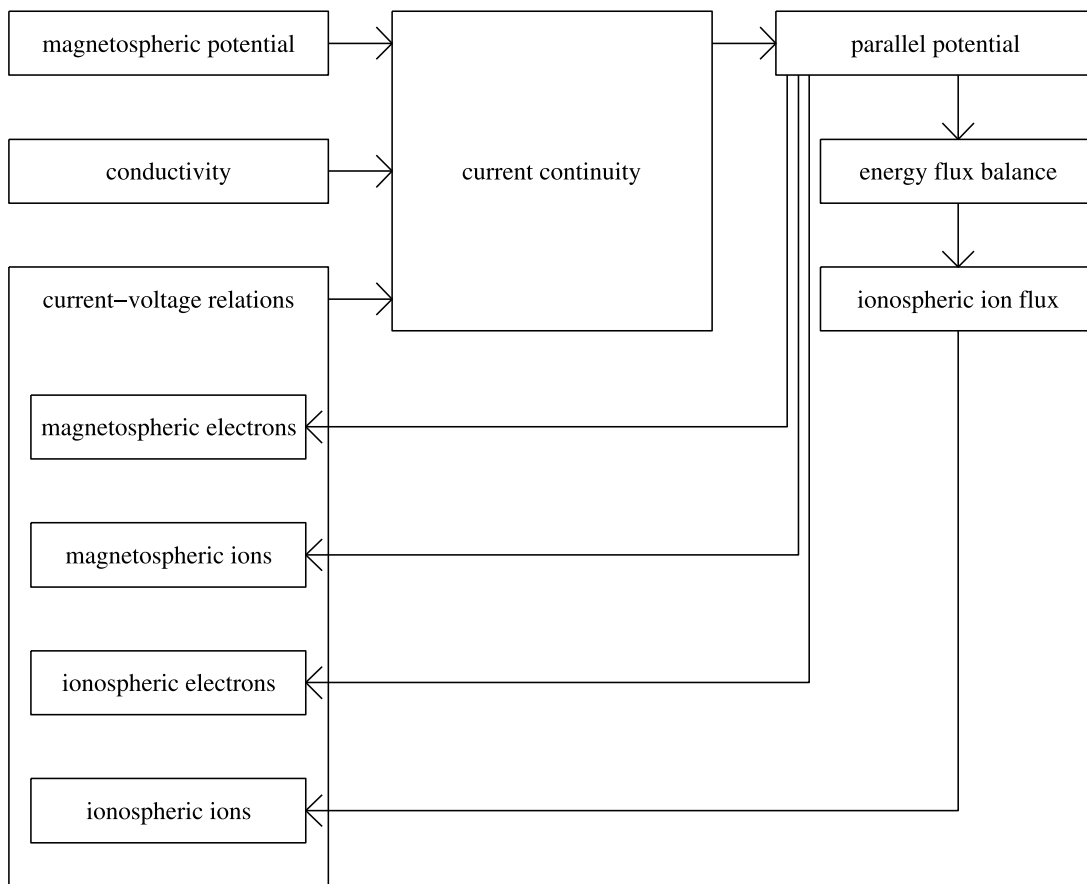


Figure 6. Scheme of the modeling procedure. The central element is the current continuity equation, which relies on three inputs: the magnetospheric potential profile, the ionospheric height-integrated Pedersen conductivity, and the field-aligned currents obtained from the current-voltage relationships for each of the participating species. Solving the current continuity equation produces the field-aligned electric potential drop. This is used in turn to improve upon the field-aligned currents. More specifically, it also allows computing of the energy input into the ionosphere and thereby constrains the number of upgoing ionospheric ions. The procedure is continued until a satisfactory fit of the observations is obtained. The parameters of the model are determined from only a few characteristics of the observed transition; the model result reproduces more properties of the transition than those directly involved in the fit.

(in this event, that is in the direction radially away from Earth), and b_t is the mapping factor along the PCB (corresponding to azimuthal distances). The magnetic latitude of Cluster-1 is given from $\hat{\lambda} = \arccos \sqrt{5.6/L} = 47.8^\circ$ and that of the ionospheric foot point is $\lambda = \arccos \sqrt{(1+h/RE)/L} = 73.0^\circ$. The azimuthal mapping factor then follows from $b_t = 5.6 \cos \hat{\lambda} / (1+h/RE) \cos \lambda = 12.1$. Knowing that $b_n b_t = B/\hat{B} = 143$, one finds that $b_n = 11.8$. Together, b_n and b_t relate the high-altitude measurements to the topside ionosphere and vice versa.

[39] The magnetospheric potential is represented here by a smooth profile that matches the observed one. Let $x' = (x - x_{\text{center}})/P$, with a transition half-width parameter $P = 64$ km at ionospheric altitude, corresponding to $\hat{P} = b_n P = 750$ km in the magnetosphere. The potential profile then is expressed as

$$\hat{\phi}(x) = \frac{\Delta_{\perp} \hat{\phi}}{2} \left[\operatorname{erf} \left(2x' \left(1 - 0.57e^{-x'^2} \right) - 0.3 \right) - 1 \right]. \quad (9)$$

[40] As indicated in Figure 6, an important ingredient of the model are the field-aligned currents (or, equivalently, the number fluxes) as obtained from the current-voltage characteristics of each participating population. Below, we systematically describe each of the current-carrying populations in terms of observations and/or simple models.

[41] The plasma sheet H^+ population has a density of $N_{H^+ \downarrow} = 0.15 \text{ cm}^{-3}$ and an energy up to $k_B T_{H^+ \downarrow} = 30$ keV. The hot O^+ ions have densities of 1% of that of the protons, compatible with the observations, and the same energies. There are about as many hot plasma sheet electrons as ions, $N_{e \downarrow} = N_{H^+ \downarrow} + N_{O^+ \downarrow}$, and their mean energy is around $k_B T_{e \downarrow} = 6$ keV. Assuming that downward moving particles are lost if they mirror below the topside ionosphere altitude h , the loss cone angle θ in the hot population as observed by Cluster-1 is found from

$$\sin^2 \theta = \frac{1}{b_n b_t}, \quad (10)$$

so that $\theta = 4.8^\circ$. Note that this is too small to be resolved in the CIS/HIA distribution of Figure 2. The loss cone covers a solid angle of $\pi \tan^2\theta = 0.022$ sr. If the hot particles would have been distributed isotropically in a spherical shell distribution, that would have amounted to a fraction $\alpha = 0.0018$ of the hot particles. Since, however, the distribution is predominantly downward, the fraction in the loss cone is larger. Based on the true shape of the observed distribution, we have estimated this fraction numerically to be $\alpha = 0.0036$. The high-altitude hot ion precipitation speed follows from $v_{i\downarrow}^2 = k_B T_{i\downarrow}$, $i = \text{H}^+, \text{O}^+$. This leads to a net downward ion number flux measured at the topside ionosphere altitude

$$f_{i\downarrow} = -b_n b_i \alpha N_{i\downarrow} v_{i\downarrow}; \quad i = \text{H}^+, \text{O}^+, \quad (11)$$

corresponding to a downward current $j_{\parallel i\downarrow} = e f_{i\downarrow}$, which varies with position with the hot ion density and temperature. This downward flux could be enhanced in the return current region where magnetospheric ions would be accelerated downward by a negative $\Delta_{\parallel}\phi$ but, as will be demonstrated below, the energy gain from such a potential difference tends to be fairly small compared to the hot ion energy and does not alter the ion precipitation much.

[42] The downward hot electron flux is more sensitive to the effects of parallel acceleration. This flux can be modeled as a combination of the flux from the particles in the loss cone and the additional electrons accelerated downward where $\Delta_{\parallel}\phi > 0$, which usually is much larger than for the return current. The flux at altitude h can be expressed as

$$f_{e\downarrow} = -b_n b_e \alpha N_{e\downarrow} v_{e\downarrow} - \frac{K_p}{e} \max\{\Delta_{\parallel}\phi, 0\}, \quad (12)$$

where $K_p = 0.35 \times 10^{-8}$ C/V m² s is the Knight constant in the corresponding linear current-voltage relation $j_{\parallel e\downarrow} = K_p \max\{\Delta_{\parallel}\phi, 0\}$ for these electrons in the upward current region. This particular value of K_p was chosen to obtain the observed upward currents of around $0.02 \mu\text{A}/\text{m}^2$ at magnetospheric altitude, for a parallel potential difference on the order of 500 V (which turns out to be the parallel potential difference that follows from the model).

[43] For the upgoing electron flux out of the ionosphere at altitude h in the return current region, the linear current-voltage relation

$$j_{\parallel e\uparrow} = K_m \min\{\Delta_{\parallel}\phi, 0\} \quad (13)$$

is adopted. This relation implies a zero current for positive $\Delta_{\parallel}\phi$ as the ionospheric electrons then cannot overcome the parallel potential barrier; a linear regime with Knight constant K_m describes the currents produced when the electrons are accelerated upward by a negative parallel potential difference. This current-voltage relation corresponds to a particle flux

$$f_{e\uparrow} = -\frac{K_m}{e} \min\{\Delta_{\parallel}\phi, 0\}. \quad (14)$$

The parameter value is chosen here as $K_m = 1.7 \times 10^{-8}$ C/V m² s, compatible with the observed strength of the return currents.

[44] The plasma sheet precipitation may excite lower hybrid waves in the upper ionosphere. These waves can lead

to a transverse heating of the ionospheric ions that may be sufficient to allow these ions to escape from the upper ionosphere [Chang and Coppi, 1981; Eliasson *et al.*, 1994]. In the model used here, the low-altitude energy of these escaping ions is considered to be constant and given: $T_{\text{H}^+\uparrow} = 200$ eV and $T_{\text{O}^+\uparrow} = 300$ eV; these values match the observed ion parallel velocities where $\Delta_{\parallel}\phi = 0$. Note that if the ion escape process would be due to acceleration through a parallel potential difference at low altitude, the H^+ and O^+ energies should be equal, so that their parallel velocities would differ by a factor $\sqrt{m_{\text{O}^+}/m_{\text{H}^+}} \approx 4$. If ion escape would be purely ballistic, their parallel velocities would both be equal to a characteristic ion escape velocity (their energies would then differ by a factor of four). The actual escape mechanism is probably somewhere in between: an O^+/H^+ energy ratio of 1.5 therefore is not surprising. A discussion of ionospheric ion energization mechanisms can be found in the review by Yau and André [1997]. The upward ion fluxes at altitude h are modeled as

$$f_{i\uparrow} = N_{i\uparrow} v_{i\uparrow}, \quad (15)$$

corresponding to a current $j_{\parallel i\uparrow} = e f_{i\uparrow}$. The energy balance in the upper ionosphere can then be used to estimate the magnitude of the upgoing ion flux and the associated current (see also Figure 6). Requiring that the upgoing ions carry a specific fraction of the energy deposited into the ionosphere by the precipitating ions and electrons, one finds

$$\begin{aligned} f_{\text{H}^+\uparrow} k_B T_{\text{H}^+\uparrow} + f_{\text{O}^+\uparrow} k_B T_{\text{O}^+\uparrow} + f_{e\uparrow} k_B T_{e\uparrow} = \\ \beta_i [f_{\text{H}^+\downarrow} (k_B T_{\text{H}^+\downarrow} - e\Delta_{\parallel}\phi) + f_{\text{O}^+\downarrow} (k_B T_{\text{O}^+\downarrow} - e\Delta_{\parallel}\phi)] \\ + \beta_e f_{e\downarrow} (k_B T_{e\downarrow} + e\Delta_{\parallel}\phi), \end{aligned} \quad (16)$$

in which β_i and β_e represent the fractions of the downward energy fluxes of the ions and the electrons, respectively, needed to produce the upward ion fluxes. The values of $\beta_i = 0.23$ and $\beta_e = 0.01$ are obtained by fitting the model to the observations, in particular by trying to reproduce the observed upgoing ion flux and its variation across the structure. Note that $|e\Delta_{\parallel}\phi| \ll k_B T_{i\downarrow}$ for the plasma sheet ions and, less so, for the plasma sheet electrons. The incident energy flux therefore depends on $\Delta_{\parallel}\phi$ mainly through $f_{e\downarrow}$. For the sake of simplicity, $T_{e\uparrow}$ is considered to be small so that the escaping electrons do not carry much energy. Assuming a fixed proportion $N_{\text{O}^+\uparrow}/N_{\text{H}^+\uparrow} = 0.8$, compatible with the observations, the upgoing ion fluxes can be computed from this energy balance.

[45] Knowing all the fluxes, the total parallel current in the right hand side of equation (8) is found as

$$j_z = e(f_{\text{H}^+\uparrow} + f_{\text{O}^+\uparrow} - f_{e\uparrow} + f_{\text{H}^+\downarrow} + f_{\text{O}^+\downarrow} - f_{e\downarrow}). \quad (17)$$

This current depends nonlinearly on $\Delta_{\parallel}\phi$.

[46] A final ingredient in the model is the height-integrated Pedersen conductivity in equation (8). This conductivity is simply taken here to be a constant 0.6 S. This value follows from $d^2\hat{\phi}/dx^2$ and the magnitude of the FACs; it is rather low but not uncommon for the PCB [e.g., Hardy *et al.*, 1987; Coumans *et al.*, 2004].

[47] Given all these ingredients, the current continuity equation can be solved numerically. As the problem is

nonlinear, a Newton-type iterative procedure has been used [see *De Keyser and Echim, 2010*].

3.2. Model Results

[48] The results of the model are shown in Figure 7. To facilitate a comparison between the model results and the observations, all quantities are given at magnetospheric altitude, and they are plotted as a function of the magnetospheric distance \hat{x} across the structure.

[49] Figure 7a gives the magnetospheric electric field \hat{E} across the PCB interface. Its magnetospheric width of 1500 km corresponds to an ionospheric thickness of about 120 km. The structure of the electric field is, of course, completely determined by the form of $\hat{\phi}$. Figure 7b plots $\hat{\phi}$ (red line) and ϕ (green line). The 40 kV potential difference $\Delta_{\perp}\hat{\phi}$ across the magnetospheric lobe–plasma sheet interface translates into the parallel potential difference $\Delta_{\parallel}\hat{\phi}$ shown in Figure 7c. The parallel potential difference is about -200 V in the return current region and $+700$ V in the upward current region. The induced magnetic field perturbations $\delta\hat{B}_y$, and the corresponding parallel currents \hat{j}_z are given in Figure 7d. The current system has $\Delta_{\parallel}\hat{\phi} < 0$ and downward currents on the lobe side, for $x < \xi$, while it has $\Delta_{\parallel}\hat{\phi} > 0$ and upward currents on the plasma sheet side, $x > \xi$. Because of the asymmetry of the PCB configuration (asymmetry of $\hat{\phi}$, different current-voltage relations on either side), the separator between upward and downward currents ξ is not located at the center of the transition, but toward the plasma sheet edge. Figure 7d gives the total parallel current (red curve), the parallel current associated with precipitating electrons (blue), with precipitating ions (green, essentially zero), with upgoing electrons (cyan), and with escaping ions (magenta). Precipitating hot electrons and upgoing ions dominate the upward current, while the return current is mostly due to the upgoing electrons. The regions of upward and downward current agree with the intense downward and upward electron fluxes in Figures 1c–1e. The parallel current profile obtained with the model is fairly similar to the profile deduced from the magnetic field variations in Figure 5d. To check the degree of local closure of the currents, we compare the upward and downward currents by evaluating the total net magnetospheric parallel current

$$\hat{J}_{\text{net}} = \int_{-\infty}^{+\infty} \hat{j}_z d\hat{x} = 0.0082 \text{ A/m} \quad (18)$$

and the total amount of parallel current in the system

$$\hat{J}_{\text{total}} = \int_{-\infty}^{+\infty} |\hat{j}_z| d\hat{x} = 0.0446 \text{ A/m}. \quad (19)$$

The upward and downward currents do not cancel each other exactly, although the imbalance $\hat{J}_{\text{net}}/\hat{J}_{\text{total}} = 0.018$ is small.

[50] The ion number flux spectrograms computed from the model (Figures 7f–7i) show the plasma sheet ions (an input to the model) as well as the upgoing ionospheric ions. The warm upgoing ion number density is given in Figure 7j. Although H^+ and O^+ ions are assumed to be produced in a fixed proportion $N_{\text{H}^+}/N_{\text{O}^+}$ at the top of the ionosphere, this proportion changes across the arc as the ions experience different amounts of acceleration: for a given flux a smaller/higher parallel speed results in a higher/lower local density.

Figure 7k gives the parallel velocity at Cluster altitude. There are two parameters influencing this parallel velocity. First, there is the initial energy $k_B T_{i\uparrow}$ corresponding to the perpendicular heating of the ionosphere as a consequence of precipitation. Because of the conservation of magnetic moment along diverging magnetic field lines, the perpendicular motion of these upgoing ions is converted into parallel motion and produces a self-focusing of the upgoing particles. Second, the ions experience a deceleration or an acceleration by the parallel electric field. The total parallel velocity can therefore be computed from

$$v_{zi\uparrow}^2 = 2\zeta(k_B T_{i\uparrow} + e\Delta_{\parallel}\hat{\phi})/m_i, \quad (20)$$

where ζ is an empirical constant. Case $\zeta = 1$ gives an upper limit, when all the ion perpendicular thermal velocity has been converted into parallel velocity and when there is no diffusion or scattering of the upgoing particles. In reality neither of both is true. Counterstreaming particle beams are likely to excite instabilities that drive wave activity and promote scattering [e.g., *Reiff et al., 1988*]. The model presented here uses $\zeta = 0.5$, which corresponds to a reduction of the bulk $v_{zi\uparrow}$ accompanied by a broadening of the parallel and perpendicular velocity distributions. The upward ion motion is accelerated/decelerated in the upward/downward current region on the plasma sheet/lobe side. Given an upgoing number flux determined by the energy deposited in the ionosphere by the precipitating hot particles, the reduced upward speed in the return current region due to the decelerating $\Delta_{\parallel}\hat{\phi} < 0$ results in a higher number density of upgoing ions there (Figure 7j). In the upward current region, where the energy $e\Delta_{\parallel}\hat{\phi}$ from the parallel acceleration dominates the low-altitude energy $k_B T_{i\uparrow}$, the proportion $v_{z\text{H}^+\uparrow}/v_{z\text{O}^+\uparrow}$ approaches the square root of the oxygen to proton mass ratio. The bulk perpendicular velocity is $\hat{v}_{\perp y\uparrow} = -\hat{E}_x/\hat{B}$ due to the electric drift, independent of mass or charge (Figure 7l). The equatorward field results in an eastward drift that matches the observed one. Since the ionospheric and magnetospheric potentials almost coincide, the ionospheric field is essentially the mapped magnetospheric electric field, $E = b_n \hat{E}$, and it therefore is an order of magnitude stronger. At the same time, however, the ionospheric magnetic field $B = b_n b_r \hat{B}$ is 2 orders of magnitude larger than the magnetospheric field, so that the drift at the topside ionosphere is $v_{\perp\uparrow} = \hat{v}_{\perp y\uparrow}/b_r$, an order of magnitude smaller than the magnetospheric drift, i.e., up to 8 km/s over a region that is a few tens of km wide. At lower altitudes in the ionosphere, however, the potential differences and the perpendicular electric field are diminished as the current system already closes partially by horizontal currents in the upper ionosphere, so that the drift velocity is further reduced.

[51] Both parallel electrostatic acceleration and the electric drift by themselves do not change the ion temperatures. That is why the upgoing ions still appear as a beam at Cluster altitude. The perpendicular velocity of the beam dominates the parallel velocity for $x < \xi$, while the opposite is true for $x > \xi$. The model therefore predicts a sharp transition in the warm ion pitch angle from perpendicular propagation ($\theta = 90^\circ$) for $x < \xi$ to parallel upward propagation ($\theta = 0^\circ$) for $x > \xi$ (Figures 7g and 7i). That is exactly what is observed (Figures 1g and 1i). Moreover, when

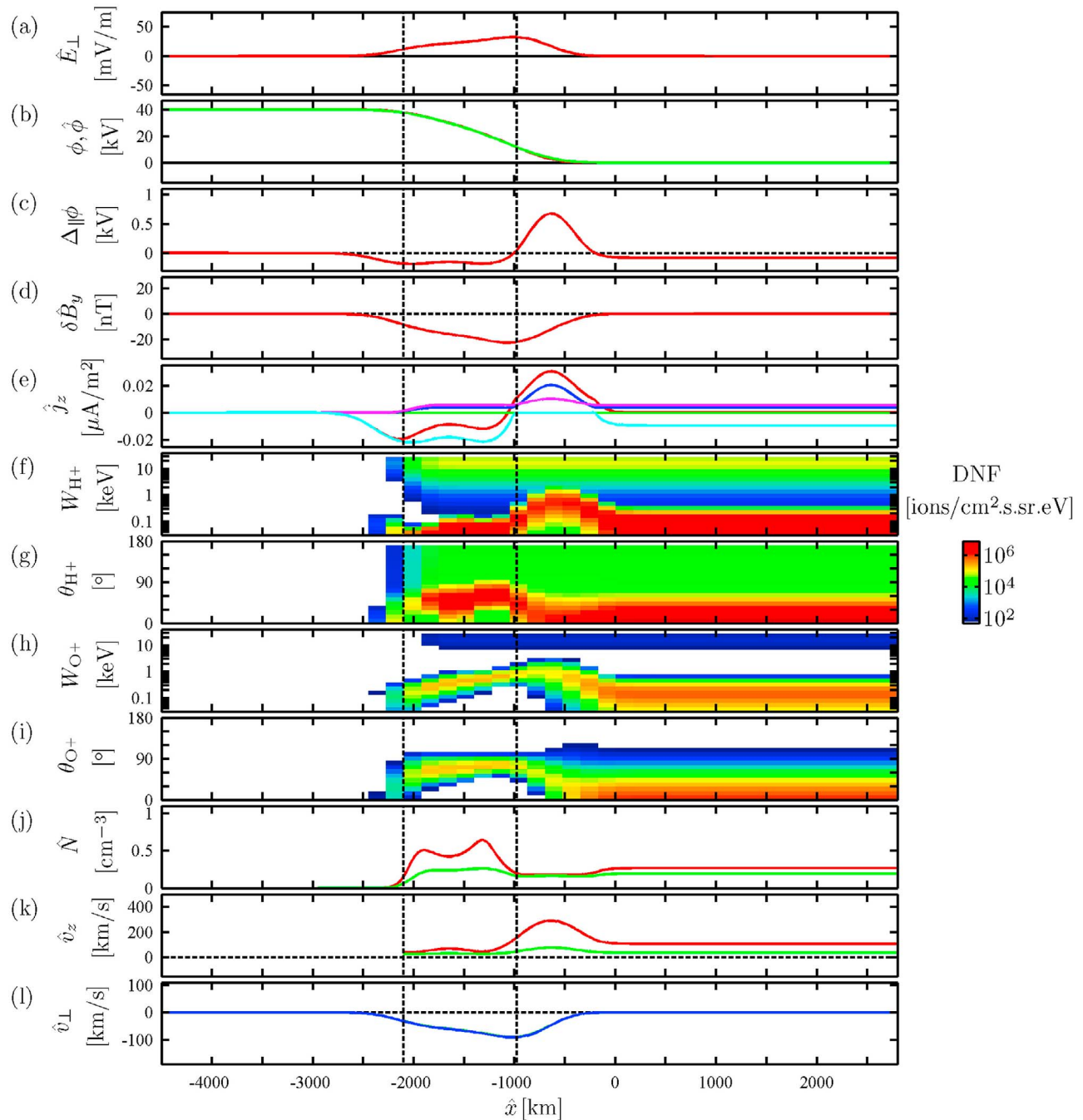


Figure 7. Polar cap boundary arc structure from a model. Magnetospheric quantities are shown as a function of the transverse coordinate \hat{x} at Cluster altitude so as to facilitate comparison with Figure 5. The drivers of the current system are the magnetospheric electric potential profile and the hot particle precipitation (see text). (a) Electric field \hat{E}_x normal to the arc. (b) Magnetospheric (red) and ionospheric (green) electric potential. (c) Parallel potential difference. (d) Magnetic field perturbation $\delta\hat{B}_y$, generated by the parallel current. (e) Parallel current carried by precipitating ions (green, but negligibly small) and electrons (blue) and by upward ions (magenta) and electrons (cyan), as well as the total current (red). H^+ differential number flux as a function of (f) energy and (g) pitch angle and O^+ differential number flux as a function of (h) energy and (i) pitch angle, using the same color scale as in Figure 1. (j) Ionospheric H^+ (red) and O^+ (green) density. (k) Parallel velocity of ionospheric H^+ (red) and O^+ (green). (l) Perpendicular velocity of ionospheric H^+ and O^+ and electric drift velocity, all coinciding (blue).

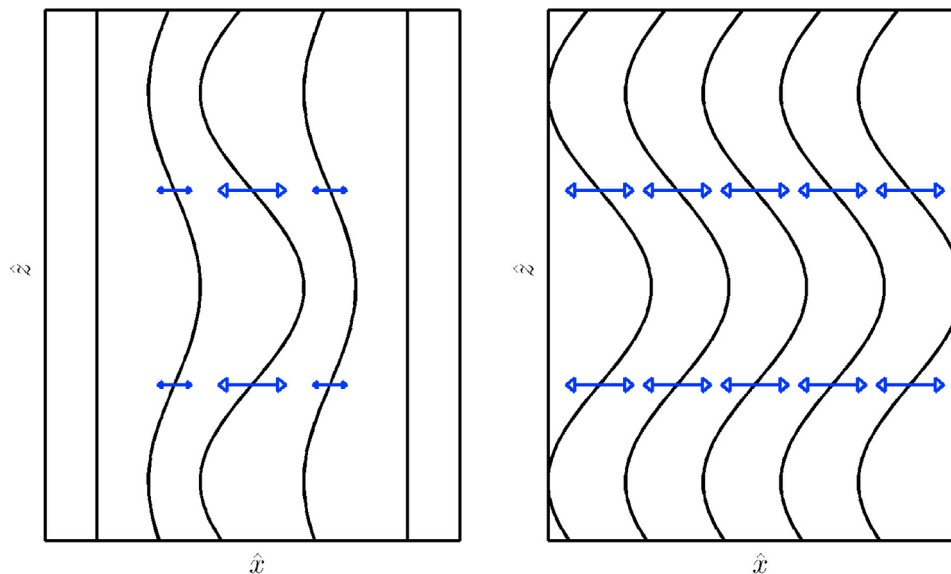


Figure 8. Two different oscillation modes of a field-aligned cold plasma boundary. (left) The boundary acts as a wave guide, with the wave confined to the layer. The wave can be characterized as a collective compressional oscillation. (right) The boundary moves as a whole as an incompressible plasma slab.

looking in more detail at the pitch angle distributions above the return current region, one observes that they are concentrated there in a range $\theta \in [\theta_{\min}, 90^\circ]$. That $\theta < 90^\circ$ corresponds to the fact that the ions move upward. The lower boundary θ_{\min} is set by the ratio $\hat{v}_{z\uparrow}/\hat{v}_{\perp\uparrow}$. Since the perpendicular velocity is the same for both ions, θ_{\min} is largest for the O^+ ions as they tend to have a smaller upward speed. In other words, the pitch angle interval is narrower for O^+ than for H^+ .

3.3. Explanatory Nature of the Model

[52] The model presented above introduces a number of parameters: K_p , K_m , $T_{H^+\uparrow}$, $T_{O^+\uparrow}$, $N_{O^+\uparrow}/N_{H^+\uparrow}$, β_i , β_e , ζ , and Σ_p . These parameters reflect a lack of direct observations and our incomplete understanding of the physics involved. Starting from a value for Σ_p and solving the model equations, the fitting procedure estimates the parameters from the following observational constraints: K_p and K_m follow from the observed maximum upward and downward field-aligned current; $T_{H^+\uparrow}$ and $T_{O^+\uparrow}$ are obtained from the observed $\hat{v}_{zH^+\uparrow}$ and $\hat{v}_{zO^+\uparrow}$ at the point where $\Delta_{\parallel}\phi = 0$; $N_{O^+\uparrow}/N_{H^+\uparrow}$ is obtained from an overall fit of $\hat{N}_{O^+\uparrow}/\hat{N}_{H^+\uparrow}$, although the latter varies over the simulation domain because of the variability of the upward warm ion speeds; β_i and β_e determine the amount of energy pumped into the upgoing ions and can therefore be obtained separately from the observed $\hat{N}_{H^+\uparrow}$ and $\hat{N}_{O^+\uparrow}$ profiles, which show variations that reflect both the precipitating ion energy input as well as the precipitating electron energy input, which is locally enhanced in the upward current region; ζ is simply set to a reasonable value. In conclusion, the model fitting is based on an initial choice of the ionospheric conductivity, a fairly direct determination of most other parameters, and a trial-and-error procedure to find the values of β_i and β_e that fit the observations best. In this way, the iterative procedure sketched in Figure 6 can be completed.

[53] The model, however, reproduces a number of observed features that have not been used in the fitting procedure, but that follow from the physics incorporated into the model. These include (1) matching the thicknesses of the upward and downward current regions to the observed ones; (2) obtaining a parallel potential difference $\Delta_{\parallel}\phi$ that matches the energies of the upgoing ionospheric ions where $\Delta_{\parallel}\phi > 0$ and of the upgoing electrons where $\Delta_{\parallel}\phi < 0$; (3) reproducing the observed H^+ and O^+ pitch angle distributions, including the transition between parallel and predominantly perpendicular propagation; (4) matching the observed perpendicular speeds of the upgoing H^+ and O^+ ions; (5) recovering the enhancement in the upward speed of the warm ions in the electron precipitation region; (6) the fact that K_p and K_m turn out to have sensible values; and (7) modeling the observations with realistic values $0 < \beta_i, \beta_e < 1$, something that is not guaranteed a priori.

[54] The fact that the electrostatic model is able to relate independent observational findings is a confirmation of the consistency of the analysis. For instance, the FACs are computed from the observed $\delta\hat{B}_y$, and through the model also from the magnetospheric electric potential inferred from \hat{E}_x , and both are found to agree. This is not evident; in particular it further suggests that our original choice of reference frame orientation was a good one. It also supports the idea that boundary motion must be accounted for in the analysis.

4. Discussion

[55] Auroral current systems have been believed to be powered by generators at magnetospheric interfaces for some time [e.g., Roth et al., 1993; De Keyser, 1999; Marghitu et al., 2006; Hamrin et al., 2006; Echim et al., 2009; De Keyser and Echim, 2010]. For PCB arcs this is

very plausible as they are associated with the lobe–plasma sheet interface, which is a permanent feature. The magnetospheric structure must be the cause and the arc the consequence, notwithstanding ionospheric feedback on the arc itself and on the magnetospheric interface.

[56] In the present paper we have found that wave-like features and electrostatic features can coexist, at least in the limit of long-period waves: the interface can then be regarded as an electrostatic structure that is moving back and forth as the spacecraft traverses it. In this context it is interesting to reexamine the waves at the boundary and the appropriateness of equation (4): is it really correct to use the locally measured velocity as a measure of boundary motion? Figure 8 depicts two possible wave modes on the interface. In the situation in Figure 8 (left), the waves remain confined to the interface, which appears to act as a waveguide. This is a compressional fast-mode type of boundary mode. This model seems to correspond to the situation observed here, where waves are only observed inside the interface. The alternative depicted in Figure 8 (right) corresponds to a boundary that is oscillating collectively as an incompressible entity; it is the latter that corresponds to the hypothesis of equation (4). In the former case, the structure is intrinsically time dependent, while in the latter case it can be regarded as an oscillating static structure. Although there is a difference between both in principle, there does not necessarily have to be a big difference in practice. The fact that a set of reasonable and consistent spatial profiles can be found seems to indicate that the approach that we have taken is indeed justified. In any case, it should be stressed that in analyzing auroral generator interfaces, motion of the boundary is an important aspect that cannot be ignored in general. Utmost care is needed when computing the parallel potential profile and the field-aligned currents.

[57] For the event analyzed here, the premise of a quasi-static current circuit appears to hold only on average as the dynamical time scale of the driver in the system, the lobe–plasma sheet boundary, is a few minutes, on the order of the Cluster-1 crossing time, while the relevant time scales of the coupled magnetosphere–ionosphere system (the time needed by Alfvén waves and particles to traverse it) range from seconds to minutes as well. Nevertheless, a quasi-electrostatic model has been used to study the event and seems to reproduce its essential properties. The parallel potential drop from the model is on the order of 0.7 kV in the upward current region, compatible with the observed maximum high-altitude energy of the upgoing ions. The model potential drop in the return current region is about –0.2 kV, compatible with the energies of accelerated electrons there, although the return current region has a more filamentary character than in our simple model as can be seen from the fine-scale structure in the observed electron spectrograms (Figures 1c–1e). The observed and modeled current densities agree because of the choice of K_p and K_m . The modeled current layer thicknesses also match the observed ones, and this is a result that follows from the solution of the current continuity differential equation. Note that the width of the upward current region is about 500 km at magnetospheric altitude, which corresponds to 40 km at ionospheric altitude, not incompatible with discrete arc thicknesses though rather wide [Knudsen *et al.*, 2001;

Johansson *et al.*, 2007]. The association between convergent/divergent electric field signatures with up/downward current regions in the auroral zone is well established [e.g., Marklund *et al.*, 1994; Johansson *et al.*, 2005, 2007]. In terms of their optical signature in the auroral ionosphere, monopolar electric fields can be regarded as a set of adjacent upward/downward current sheets, possibly related to visible optical emissions in the upward current region and to black aurora in the downward current region.

[58] Consider the ionospheric ions. They are forced to move with the ionospheric $\vec{E} \times \vec{B}$ drift. Wherever there is plasma sheet precipitation, transverse ion heating by lower hybrid waves [Eliasson *et al.*, 1994] heats the ionospheric ions sufficiently so as to allow them to flow upward. Because of the conservation of magnetic moment, the initial ion perpendicular temperature at low altitude is progressively converted into upward field-aligned motion as well, but this adiabatic process does not change the particle energy. It does, of course, produce an acceleration of the ion parallel velocity. As the ions move up, they also experience a perpendicular energization as the electric drift increases progressively with height. In addition, the ions gain/lose parallel energy in the upward/return current region as they are accelerated/decelerated by the parallel potential difference. This explains the marked transition in the warm ion pitch angles from $\theta = 90^\circ$ to 0° on the equatorward edge of the monopolar electric field region. The model also predicts a unidirectional eastward flow along the arc as an ionospheric signature of PCB arcs, which is directly related to the monopolar nature of the electric field [Kullen *et al.*, 2008].

[59] Hot plasma sheet particle precipitation appears to offer an ample source of energy for the outflow of ionospheric ions with ~ 100 eV, as evidenced by the small energy flux fractions β_i and β_e needed in the model. Especially the electron contribution to the direct heating of ions in the upper ionosphere is limited, since the electrons penetrate deeply in the ionosphere and produce auroral emission there.

[60] In summary, the quasi-static model does a good job at explaining the observations. The specific shape of the ionospheric potential profile, and hence of the parallel potential difference and of the parallel currents, depends strongly on the conductivity profile and on the magnetospheric potential. For instance, relatively small fluctuations in the ϕ profile on the order of 100 eV produce significant changes in the precipitation pattern and in the parallel current distribution. The major characteristics of the solution obtained here, however, remain unchanged: the current system associated with monopolar electric fields consists always of a pair of upward/downward current sheets, and the upgoing ions bear the imprint of the different contributions of the parallel and perpendicular energization mechanisms.

[61] The quasi-static description used here is, however, far from complete. A proper understanding of polar cap boundary arcs would require detailed modeling of the ionospheric conductivity, of the transverse ion heating process and of the escape of the ions from the ionosphere, of the dynamics of the counterpropagating particles in both upward and downward current regions and the corresponding effects on the

current–voltage relation, and of the kinetic structure of the lobe–plasma sheet generator.

[62] **Acknowledgments.** The authors thank Y. Voitenko for helpful discussions. The authors acknowledge the support by the Cluster Active Archive and by the EFW, FGM, CIS, and PEACE teams, who provided the data. This work was funded by the Belgian Science Policy Office through Prodex/Cluster (PEA 90316) and the Belgian Solar–Terrestrial Centre of Excellence.

[63] Robert Lysak thanks the reviewers for their assistance in evaluating this paper.

References

- Aikio, A. T., T. Pitkänen, A. Kozlovsky, and O. Amm (2006), Method to locate the polar cap boundary in the nightside ionosphere and application to a substorm event, *Ann. Geophys.*, *24*, 1905–1917, doi:10.5194/angeo-24-1905-2006.
- Aikio, A. T., T. Pitkänen, D. Fontaine, I. Dandouras, O. Amm, A. Kozlovsky, A. Vaivadas, and A. Fazakerley (2008), EISCAT and Cluster observations in the vicinity of the dynamical polar cap boundary, *Ann. Geophys.*, *26*, 87–105, doi:10.5194/angeo-26-87-2008.
- Atkinson, G. (1970), Auroral arcs: Result of the interaction of a dynamic magnetosphere with the ionosphere, *J. Geophys. Res.*, *75*, 4746–4755.
- Balogh, A., et al. (1997), The Cluster Magnetic Field Investigation, *Space Sci. Rev.*, *79*, 65–91.
- Balogh, A., et al. (2001), The Cluster Magnetic Field Investigation: Overview of in-flight performance and initial results, *Ann. Geophys.*, *19*, 1207–1217.
- Chang, T., and B. Coppi (1981), Lower hybrid acceleration and ion evolution in the suprathermal region, *Geophys. Res. Lett.*, *8*, 1253–1256, doi:10.1029/GL008i012p01253.
- Chaston, C. C., J. W. Bonnell, C. W. Carlson, J. P. McFadden, R. C. Ergun, R. J. Strangeway, and E. J. Lund (2004), Auroral ion acceleration in dispersive Alfvén waves, *J. Geophys. Res.*, *109*, A04205, doi:10.1029/2003JA010053.
- Chiu, Y. T., and J. M. Cornwall (1980), Electrostatic model of a quiet auroral arc, *J. Geophys. Res.*, *85*, 543–556.
- Chiu, Y. T., and M. Schulz (1978), Self-consistent particle and parallel electrostatic field distributions in the magnetospheric-ionospheric auroral region, *J. Geophys. Res.*, *83*, 629–642.
- Coumans, V., J.-C. Gérard, B. Hubert, M. Meurant, and S. B. Mende (2004), Global auroral conductance distribution due to electron and proton precipitation from IMAGE-FUV observations, *Ann. Geophys.*, *22*, 1595–1611.
- De Keyser, J. (1999), Formation and evolution of subauroral ion drifts in the course of a substorm, *J. Geophys. Res.*, *104*, 12,339–12,350.
- De Keyser, J., and M. Echim (2010), Auroral and sub-auroral phenomena: An electrostatic picture, *Ann. Geophys.*, *28*, 633–650, doi:10.5194/angeo-28-633-2010.
- De Keyser, J., M. Roth, M. W. Dunlop, H. Rème, C. J. Owen, and G. Paschmann (2005), Empirical reconstruction and long-duration tracking of the magnetospheric boundary in single- and multi-spacecraft contexts, *Ann. Geophys.*, *23*, 1355–1369, doi:10.5194/angeo-23-1355-2005.
- De Keyser, J., R. Maggiolo, and M. Echim (2010), Monopolar and bipolar auroral electric fields and their effects, *Ann. Geophys.*, *28*, 2027–2046, doi:10.5194/angeo-28-2027-2010.
- Dunlop, M. W., A. Balogh, K.-H. Glassmeier, and P. Robert (2002), Four-point Cluster application of magnetic field analysis tools: The Curlometer, *J. Geophys. Res.*, *107*(A11), 1385, doi:10.1029/2001JA005089.
- Echim, M., M. Roth, and J. De Keyser (2007), Sheared magnetospheric plasma flow and discrete auroral arcs: A quasi-static model based on kinetic theory, *Ann. Geophys.*, *25*, 317–330.
- Echim, M. M., M. Roth, and J. De Keyser (2008), Ionospheric feedback effects on the quasi-static coupling between LLBL and postnoon/evening discrete auroral arcs, *Ann. Geophys.*, *26*, 913–928.
- Echim, M. M., R. Maggiolo, M. Roth, and J. De Keyser (2009), A magnetospheric generator driving ion and electron acceleration and electric currents in a discrete auroral arc observed by Cluster and DMSP, *Geophys. Res. Lett.*, *36*, L12111, doi:10.1029/2009GL038343.
- Eliasson, L., et al. (1994), Freja observations of heating and precipitation of positive ions, *Geophys. Res. Lett.*, *21*, 1911–1914.
- Engwall, E., A. I. Eriksson, M. André, I. Dandouras, G. Paschmann, J. Quinn, and K. Torkar (2006), Low-energy (order 10 eV) ion flow in the magnetotail lobes inferred from spacecraft wake observations, *Geophys. Res. Lett.*, *33*, L06110, doi:10.1029/2005GL025179.
- Ergun, R. E., C. W. Carlson, J. P. McFadden, F. S. Mozer, G. T. Delory, W. J. Peria, C. C. Chaston, and M. Temerin (1998), FAST satellite observations of electric field structures in the auroral zone, *Geophys. Res. Lett.*, *25*, 2025–2028.
- Fridman, M., and J. Lemaire (1980), Relationship between auroral electron fluxes and field-aligned electric potential differences, *J. Geophys. Res.*, *85*, 664–670.
- Gustafsson, G., et al. (2001), First results of electric field and density observations by Cluster EFW based on initial months of observations, *Ann. Geophys.*, *19*, 1219–1240.
- Haaland, S., G. Paschmann, M. Förster, J. Quinn, R. Torbert, H. Vaith, P. Puhl-Quinn, and C. Kletzing (2008), Plasma convection in the magnetotail lobes: Statistical results from Cluster EDI measurements, *Ann. Geophys.*, *26*, 2371–2382, doi:10.5194/angeo-26-2371-2008.
- Hamrin, M., et al. (2006), Observations of concentrated generator regions in the nightside magnetosphere by Cluster/FAST conjunctions, *Ann. Geophys.*, *24*, 637–649.
- Hardy, D. A., M. S. Gussenhoven, R. Raistrick, and W. J. McNeil (1987), Statistical and functional representations of the pattern of auroral energy flux, number flux, and conductivity, *J. Geophys. Res.*, *92*, 12,275–12,294, doi:10.1029/JA092iA11p12275.
- Hubert, B., A. T. Aikio, O. Amm, T. Pitkänen, K. Kauristie, S. E. Milan, S. W. H. Cowley, and J.-C. Gérard (2010), Comparison of the open-closed field line boundary location inferred using IMAGE-FUV S112 images and EISCAT radar observations, *Ann. Geophys.*, *28*, 883–892, doi:10.5194/angeo-28-883-2010.
- Johansson, T., T. Karlsson, G. Marklund, S. Figueiredo, P.-A. Lindqvist, and S. Buchert (2005), A statistical study of intense electric fields at 4–7 R_E geocentric distance using Cluster, *Ann. Geophys.*, *23*, 2579–2588.
- Johansson, T., G. Marklund, T. Karlsson, S. Liléo, P.-A. Lindqvist, A. Marchaudon, H. Nilsson, and A. Fazakerley (2006), On the profile of intense high-altitude auroral electric fields at magnetospheric boundaries, *Ann. Geophys.*, *24*, 1713–1723.
- Johansson, T., G. Marklund, T. Karlsson, S. Liléo, P.-A. Lindqvist, H. Nilsson, and S. Buchert (2007), Scale sizes of intense auroral electric fields observed by Cluster, *Ann. Geophys.*, *25*, 2413–2425.
- Johnstone, A. D., et al. (1997), PEACE: A Plasma Electron And Current Experiment, *Space Sci. Rev.*, *79*, 351–398.
- Keiling, A. (2009), Alfvén waves and their roles in the dynamics of the Earth’s magnetotail: A review, *Space Sci. Rev.*, *142*, 73–156, doi:10.1007/s11214-008-9463-8.
- Knight, S. (1973), Parallel electric fields, *Planet. Space Sci.*, *21*, 741–750.
- Knudsen, D. J. (2001), Structure, acceleration, and energy in auroral arcs and the role of Alfvén waves, *Space Sci. Rev.*, *95*, 501–511.
- Knudsen, D. J., E. F. Donovan, L. L. Cogger, B. Jackel, and W. D. Shaw (2001), Width and structure of mesoscale optical auroral arcs, *Geophys. Res. Lett.*, *28*, 705–708.
- Kullen, A., S. Buchert, T. Karlsson, T. Johansson, S. Liléo, A. Eriksson, H. Nilsson, A. Marchaudon, and A. N. Fazakerley (2008), Plasma transport along discrete auroral arcs and its contribution to the ionospheric plasma convection, *Ann. Geophys.*, *26*, 3279–3293.
- Lemaire, J., and M. Scherer (1973), Plasma sheet particle precipitation: A kinetic model, *Planet. Space Sci.*, *21*, 281–289.
- Lyons, L. R. (1980), Generation of large-scale regions of auroral currents, electric potentials and precipitation by the divergence of the convection electric field, *J. Geophys. Res.*, *85*, 17–24.
- Lyons, L. R. (1981), Discrete aurora as the direct result of an inferred high altitude generating potential distribution, *J. Geophys. Res.*, *86*, 1–8.
- Lysak, R. (1986), Coupling of the dynamic ionosphere to auroral flux tubes, *J. Geophys. Res.*, *91*, 7047–7056.
- Lysak, R., and Y. Song (2002), Energetics of the ionospheric feedback interaction, *J. Geophys. Res.*, *107*(A8), 1160, doi:10.1029/2001JA000308.
- Marghitu, O., et al. (2006), Experimental investigation of auroral generator regions with conjugate Cluster and FAST data, *Ann. Geophys.*, *24*, 619–635.
- Marklund, G., L. Blomberg, C.-G. Fälthammar, and P.-A. Lindqvist (1994), On intense diverging electric fields associated with black aurora, *Geophys. Res. Lett.*, *21*, 1859–1862.
- Mozer, F. S., and A. Hull (2001), Origin and geometry of upward parallel electric fields in the auroral acceleration region, *J. Geophys. Res.*, *106*, 5763–5778.
- Newell, P. T., T. Sotirelis, and S. Wing (2010), Seasonal variations in diffuse, monoenergetic, and broadband aurora, *J. Geophys. Res.*, *115*, A03216, doi:10.1029/2009JA014805.
- Paschmann, G., B. U. Ö. Sonnerup, I. Papamastorakis, W. Baumjohann, N. Sckopke, and H. Lühr (1990), The magnetopause and boundary layer for small magnetic shear: Convection electric fields and reconnection, *Geophys. Res. Lett.*, *17*, 1829–1832.

- Paschmann, G., et al. (2001), The electron drift instrument on Cluster: Overview of first results, *Ann. Geophys.*, *19*, 1273–1288, doi:10.5194/angeo-19-1273-2001.
- Reiff, P. H., H. L. Collin, J. D. Craven, J. L. Burch, J. D. Winningham, E. G. Shelley, L. Frank, and M. Friedman (1988), Determination of auroral electrostatic potential using high- and low-altitude particle distributions, *J. Geophys. Res.*, *93*, 7441–7465.
- Rème, H., et al. (2001), First multi-spacecraft ion measurements in and near the Earth's magnetosphere with the identical Cluster ion spectrometry (CIS) experiment, *Ann. Geophys.*, *19*, 1303–1354.
- Rönnmark, K., and M. Hamrin (2000), Auroral electron acceleration by Alfvén waves and electrostatic field, *J. Geophys. Res.*, *105*, 25,333–25,344.
- Roth, M., D. S. Evans, and J. Lemaire (1993), Theoretical structure of a magnetospheric plasma boundary: Application to the formation of discrete auroral arcs, *J. Geophys. Res.*, *98*, 11,411–11,423.
- Sato, T. (1978), A theory of quiet auroral arcs, *J. Geophys. Res.*, *83*, 1042–1048.
- Semeter, J., C. J. Heinselman, J. P. Thayer, R. A. Doe, and H. U. Frey (2003), Ion upflow enhanced by drifting F-region plasma structure along the nightside polar cap boundary, *Geophys. Res. Lett.*, *30*(22), 2139, doi:10.1029/2003GL017747.
- Siscoe, G. L., and T. S. Huang (1985), Polar cap inflation and deflation, *J. Geophys. Res.*, *90*, 543–547, doi:10.1029/JA090iA01p00543.
- Tsurutani, B. T., J. K. Arballo, C. Galvan, L. D. Zhang, X. Zhou, G. S. Lakhina, T. Hada, J. S. Pickett, and D. A. Gurnett (2001), Polar cap boundary layer waves: An auroral zone phenomenon, *J. Geophys. Res.*, *106*, 19,035–19,056, doi:10.1029/2000JA003007.
- Tung, Y., C. W. Carlson, J. P. McFadden, D. M. Klumpar, G. K. Parks, W. J. Peria, and K. Liou (2001), Auroral polar cap boundary ion conic outflow observed on FAST, *J. Geophys. Res.*, *106*, 3603–3614, doi:10.1029/2000JA900115.
- Vaivads, A., et al. (2003), What high altitude observations tell us about the auroral acceleration: A Cluster/DMSP conjunction, *Geophys. Res. Lett.*, *30*(3), 1106, doi:10.1029/2002GL016006.
- Vedin, J., and K. Rönnmark (2005), Electrostatic potentials in the downward auroral current region, *J. Geophys. Res.*, *110*, A08207, doi:10.1029/2005JA011083.
- Weber, E. J., J. F. Vickrey, C. J. Heinselman, H. Gallagher, L. Weiss, R. A. Heelis, and M. C. Kelley (1991), Coordinated radar and optical measurements of stable auroral arcs at the polar cap boundary, *J. Geophys. Res.*, *96*, 17,847–17,863, doi:10.1029/91JA01830.
- Yau, A. W., and M. André (1997), Sources of ion outflow, *Space Sci. Rev.*, *80*, 1–25.

I. Dandouras, CESR-CNRS, F-31028 Toulouse, France. (iannis.dandouras@cesr.fr)

J. De Keyser, M. Echim, and R. Maggiolo, Space Physics Division, Belgian Institute for Space Aeronomy, Ringlaan 3, B-1180 Brussels, Belgium. (johan.dekeyser@aeronomie.be; marius.echim@aeronomie.be; romain.maggiolo@aeronomie.be)